Journal of Applied Fluid Mechanics, Vol. 14, No. 3, pp. 753-767, 2021.
Available online at www.jafmonline.net, ISSN 1735-3572, EISSN 1735-3645.
DOI: 10.47176/jafm.14.03.31722

A Numerical Investigation on the Equivalence of Shock−Wave/ Boundary-Layer Interactions using a Two Equations RANS Model

B. John† and P. Vivekkumar

School of Mechanical Engineering, Vellore Institute of Technology (VIT), Vellore, Tamil Nadu, 632 014, India

†*Corresponding Author Email*: *bibin.john@vit.ac.in*

(Received April 17, 2020; accepted October 10, 2020)

ABSTRACT

A detailed numerical investigation of two different modes of shock wave-turbulent boundary layer interaction (SWBLI) is presented. Equivalence of ramp induced SWBLI (R-SWBLI), and impingement shock based SWBLI (I-SWBLI) is explored from the computational study using an in-house developed compressible flow solver. Multiple flow deflection angles and ramp angles are employed for this study. For all the investigated cases, a freestream Mach number of 2.96 and Reynolds number of $3.47\times10^7 m^{-1}$ are considered. The $k-\varepsilon$ model with the improved wall function of present solver predicted wall pressure distributions and separation bubble sizes very close to the experimental measurements. However, the separation bubble size is slightly over overpredicted by the $k-\omega$ model in most of the cases. The effect of overall flow deflection angle and upstream boundary layer thickness on the SWBLI phenomenon is also studied. A nearly linear variation in separation bubble size is observed with changes in overall flow deflection angle and upstream boundary layer thickness. However, the equivalence of SWBLI is noted to be independent of these two parameters. The undisturbed boundary thickness at the beginning of the interaction is identified as the most adequate scaling parameter for the length of the separated region.

Keywords: Shock waves; Computational study; SWBLI-Equivalence; Turbulence modelling; Finite Volume Method; Boundary layer; Flow separation.

NOMENCLATURE

C_f	skin friction coefficient
k	specific turbulence kinetic energy
L_b	separation bubble size/length of the separated region
L_{ui}	upstream influence extent
p	local static pressure
p_∞	freestream static pressure
q_i	heat flux vector
S	distance from flat plate leading edge
t	time
T	temperature
u_{ij}	velocity vector
u_τ	frictional velocity
x_i	position vector
X	horizontal distance
X_S	point of boundary layer separation
X_o	origin/centre of interaction
X_R	point of boundary layer reattachment
X_{ui}	point of upstream influence/beginning of interaction
Y	vertical distance
α_R	compression corner angle
α_{SG}	shock generator angle
α_{equ}	equivalent flow deflection angle
δ_{ij}	Kronecker delta function
δ_o	undisturbed boundary layer thickness
ὸ	dissipation rate
ρ	density
μ	molecular viscosity
μ_T	eddy viscosity
ω	specific dissipation rate
τ_{ij}	specific Reynolds-stress tensor

1. INTRODUCTION

For increasing Mach numbers, characterizingshock-wave/boundary-layer interactions (SWBLI) becomes progressively more important to the design of supersonic vehicles. The adverse pressure gradient induced by SWBLI can potentially determine the flow separation, total pressure loss, increased unsteadiness, intake un-start etc. These effects are more or less similar in different kinds of SWBLIs. The types of SWBLI differ in terms of their means of occurrence. SWBLI is often due to presence of compression ramps, impingement of shock into the boundary layer and due to the appearance of forward or backward facing steps (Babinsky and Harvey 2011). The schematic diagram representing different modes of SWBLI is given in Fig.1.

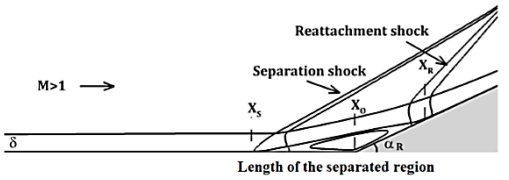

(a)

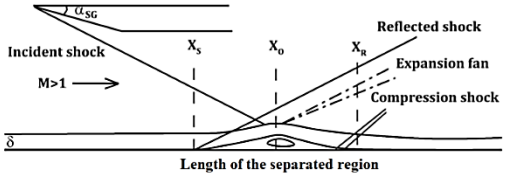

(b)

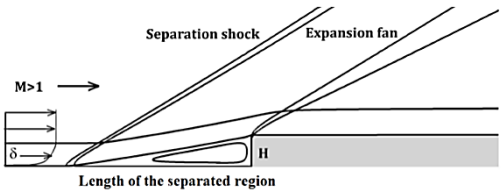

(c)

Fig. 1. Schematic representation of different types of SWBLIs (a) Ramp induced (b) Incident shock based and (c) step induced.

Shock wave boundary layer interaction research has more than 70 years of history. In the mid 1940s Liepmann (1946) experimentally studied the effect of shock wave boundary layer interactions (SWBLI) in a transonic flow over a circular arc profile. The experiment revealed that the laminar/turbulent nature of the boundary layer has significant effect on the shock pattern created and the pressure distribution over the air-foil surface. Also for a fixed freestream Mach number, changing the boundary layer profile from laminar to turbulent one resulted in notable variation in its shock pattern and the wall pressure distribution. Later, Chapman *et al*. (1958) performed a series of experimental studies to understand the phenomenon of SWBLI resulted boundary layer flow separation. Various geometries like steps, bases, curved surfaces, compression corners, etc. were considered in this exhaustive study. This study showed that the pressure rise to separation in turbulent flow is independent of the source/mode of interaction. Shock wave boundary layer interaction in the presence of forward-facing step has been investigated by Zukoski (1967) in 1967. The influence of Mach number, Reynolds number and step height on the plateau-pressure within the separation zone was the prime focus of this study. The scaled plateau pressure was proven to be independent of the Reynolds number in turbulent flows. Zukoski (1967) and later, several other researchers have identified that the separated region length is proportional to the height of the boundary layer thickness just upstream of the interaction zone.

Comparison of SWBLI parameters obtained with different modes of shock wave boundary layer interactions was also carried out by few researchers in this field. An effort to explore the equivalence of two different types of SWBLIs can be seen in the work of Law (1976). According to this study, the surface pressure distributions of impingement shock based SWBLI and ramp induced SWBLI can be the same when the overall flow deflection is the same in both cases. Based on this work, later Delery (Babinsky and Harvey 2011) has concluded that the boundary layer responds to the adverse pressure gradient imposed by the SWBLI in the same manner regardless of the cause of interaction. Surface heat flux variation caused due to SWBLI has also been studied by many researchers, all such early studies are summarized in the review article by Korkegi (1971). According to Holden (1977), the shock wave boundary layer interactions in hypersonic flows can lead to excess surface heating due to the reattachment of the separated shear layer back on the surface. Holden's study indicated that the peak heatflux of an interaction resulting in a local flow separation is much higher than that obtained for a SWBLI without separation. Such elevated surface heatflux values may cause the disintegration of the vehicle structure. So proper care needs to be taken during material selection to withstand this severe heat transfer scenario. Empirical correlations and scaling laws for the prediction of SWBLI parameters were also developed by few investigators in this field (Holden (1977), Katzer (1989), Davis and Sturtevant (2000), John and Kulkarni (2014)). Very strong I-SWBLIs occurring near the leading edge of flat plates were experimentally studied by Sriram *et al*. (2016). Based on the experimental observations, an inviscid scaling law for the length of the separation region created on a flat plate with a sharp leading edge was proposed. A linear dependency of separation length and the reattachment pressure ratio was the major finding of this work. Recently, Zhou *et al*. (2019) conducted exhaustive numerical studies to propose scaling laws for the prediction of separation length of shock wave boundary layer interactions. The incident shock- boundary layer interactions occurring at diverse freestream conditions were investigated. Scaling laws for the length of the separated region of low and high Mach numbers were devised separately.

Almost all the past studies showed the occurrence of local flow separation when the given SWBLI condition satisfies the incipient separation condition.

Therefore, Delery (1985) carried out a detailed review of the various control techniques to minimize the zone of separation in the presence of SWBLI. The separated bubble can be minimized by various active and passive control techniques. Detailed discussion on the physics of different SWBLI cases and possible SWBLI control techniques can also be noted from reporting (Delery (1985), Babinsky and Ogawa (2008), Zhang *et al*. (2014)) of other established researchers in this field. In addition to a large pool of experimental studies, a considerable amount of numerical study of SWBLIs has also been taken place in the last two decades, among which several earlier studies (Bodonyi and Smith (1986), Degrez *et al*. (1987), Grasso and Marini (1996)) were looking at the interaction of shock waves and laminar boundary layers. With the subsequent developments in the computational techniques, researchers have expanded the numerical framework to turbulent flows as well. Both Direct Numerical Simulation (DNS) and Large Eddy Simulation (LES) frameworks have been employed successfully to study SWBLIs (Pirozzoli and Grasso (2006), Garnier *et al*. (2002), Aubard *et al*. (2013)). The Direct Numerical Simulation is capable of resolving complete scales of the turbulence Moin and Mahesh (1998) , therefore it can be employed as the most accurate tool for the study of shock wave boundary layer interaction involving transition. On the other hand, Large eddy simulations directly resolve only the significant/ large scale eddies and model the effects of the small scales Meneveau and Katz (2000). Although LES ignore the direct resolving of the contribution of small eddies to the overall turbulence statics of the flow, this technique is also equally good in the study of SWBLIs Nichols *et al*. (2017). However, the above mentioned high fidelity numerical techniques are computationally more expensive, and implementation of them pose a lot of challenges in resolving the small-scale turbulence with least numerical dissipation. Further, DNS and LES simulations are inevitable only when the capturing of unsteadiness involved in the SWBLI is of primary focus Zuo *et al*. (2019). On the other hand, Reynolds averaged Navier-Stokes (RANS) modeling using one-equation or two-equation models are proved to be computationally cheaper in comparison with LES and DNS. However, these simplified models cannot predict the eddies Celik (2005), rather they are good in predicting average turbulent flow structure in a quick manner. In most of the cases, preliminary design of space vehicle configuration necessitates only accurate prediction of overall flow structure. This fact is equally applicable to the numerical prediction of SWBLI phenomenon. The RANS models are preferred over DNS/LES when the steady flow simulations are the focus of interest Knight *et al*. (2003). The literature reported RANS models range from algebraic to the Reynolds stress models. Two equation models are more powerful and accurate than algebraic and one equation models due to the fact that they additionally solve two distinct transport equations Catalano and Amato (2003). Therefore, the complete calculation of Reynolds stress tensor is possible by using mean turbulent parameters and local state of the mean flow. However, each two-equation turbulence model has it's own pros and cons when employed for the simulation of particular fluid flow scenario Christopher and Frederick (2006). Further, it is important to numerically re-investigate the equivalence of different kinds of SWBLIs to visualize and completely reveal the experimentally observed equivalent nature of ramp induced and shock impingement based SWBLIs. Therefore, the objective of the present work is to evaluate the accuracy of $k-\varepsilon$ and $k-\omega$ solvers in resolving the SWBLI. Besides the similarity between an oblique shock impinging on a flat plate and a compression ramp with an equivalent inviscid jump in pressure, it is necessary to prove which solver performs the best in resolving the two aforementioned problems. Additionally, the present study rechecks the correctness of usage of upstream undisturbed boundary layer thickness as the scaling parameter for separation bubble.

2. METHODOLOGY

To investigate the shock wave-boundary interaction in a turbulent supersonic flow, a finite volume compressible flow Navier-Stokes solver has been developed in-house by following 2D unstructured framework. The mass, momentum and energy equations considered for the present solver development are, Continuity equation:

$$\frac{\partial \rho}{\partial t}+\frac{\partial}{\partial x_i}(\rho u_i)=0$$

Momentum equation:

$$\frac{\partial}{\partial t}(\rho u_i)+\frac{\partial}{\partial x_j}\left(\rho u_j u_i+p\delta_{ij}-\tau_{ij}\right)=0$$

Energy equation:

$$\frac{\partial}{\partial t}(\rho E)+\frac{\partial}{\partial x_i}\left[\left(\rho u_i\left(E+\frac{p}{\rho}\right)-\tau_{ij}u_{ij}+q_i\right)\right]=0$$

In order to construct the correlation between the thermodynamic variables (p,ρ,T), the ideal gas law equation $p=\rho RT$ is used here. Since the present solver is a two-equation turbulent flow solver, in addition to the above equations, two more equations are to be considered to resolve the turbulence characteristics of the flow-field. The corresponding turbulence equations of $k-\omega$ Wilcox (1998) and $k-\varepsilon$ Launder and Spalding (1972) models are given below.

***k − ω* model:**

Turbulence kinetic energy equation (k):

$$\frac{\partial}{\partial t}(\rho k)+\frac{\partial}{\partial x_j}\left(\rho k u_j\right)=\rho\tau_{ij}\frac{\partial u_i}{\partial x_j}-\rho\beta^* f_{\beta^*}\mathbf{k}\,\omega+\frac{\partial}{\partial x_j}\left[\left(\mu+\frac{\mu_T}{\sigma_k}\right)\frac{\partial \mathbf{k}}{\partial x_j}\right] \quad (1)$$

Specific dissipation rate equation (ω):

$$\frac{\partial}{\partial t}(\rho\omega)+\frac{\partial}{\partial x_j}(\rho\omega u_j)=\alpha\frac{\omega}{k}\rho\tau_{ij}\frac{\partial u_i}{\partial x_j}-\rho\beta\,\omega^2 +\sigma_d\frac{\rho}{\omega}\frac{\partial k}{\partial x_j}\frac{\partial\omega}{\partial x_j}+\frac{\partial}{\partial x_j}\left[\left(\mu+\frac{\mu_T}{\sigma_\omega}\right)\frac{\partial\omega}{\partial x_j}\right] \quad (2)$$

Where,

$$\mu_T=\frac{\rho k}{\omega},\beta^*=\beta_i^*\left[1+\zeta^* F(M_T)\right]$$

$$\beta_i^*=\beta_\infty^*\left[\frac{\frac{4}{15}+\left(\frac{Re_T}{Re_\beta}\right)^4}{1+\left(\frac{Re_T}{Re_\beta}\right)^4}\right]$$

$$\beta=\beta_i\left[1-\frac{\beta_i^*}{\beta_i}\zeta^* F(M_T)\right],M_T{}^2=\frac{2k}{a^2}$$

$$Re_T=\frac{\rho k}{\mu\omega},a=\sqrt{\gamma RT}$$

$$f_{\beta^*}=\begin{cases}1 & \chi_k\le 0\\ \dfrac{1+680\chi_k{}^2}{1+400\chi_k{}^2} & \chi_k\le 0\end{cases},\chi_k=\frac{1}{\omega^3}\frac{\partial k}{\partial x_j}\frac{\partial\omega}{\partial x_j}$$

$$f_{\beta^*}=\begin{cases}1 & \chi_k\le 0\\ \dfrac{1+680\chi_k{}^2}{1+400\chi_k{}^2} & \chi_k\le 0\end{cases},\chi_k=\frac{1}{\omega^3}\frac{\partial k}{\partial x_j}\frac{\partial\omega}{\partial x_j}$$

$$F(M_T)=\begin{cases}0 & M_T\le M_{T_o}\\ M_T{}^2-M_{T_o}{}^2 & M_T>M_{T_o}\end{cases}$$

$$\sigma_d=\begin{cases}0 & \frac{\partial k}{\partial x_j}\frac{\partial\omega}{\partial x_j}\le 0\\ \sigma_{do} & \frac{\partial k}{\partial x_j}\frac{\partial\omega}{\partial x_j}>0\end{cases},$$

$$\alpha=\frac{13}{25},Re_k=6.0,\beta_i=0.072,\sigma_k=2.0,$$

$$R_\omega=2.95,\sigma_\omega=2.0,\sigma_{do}=1.5,\zeta^*=1.5,$$

$$Re_\beta=8.0,\beta_\infty^*=0.09,M_{T_o}=0.25,\gamma=2.0$$

$k-\varepsilon$ model:

Turbulence kinetic energy equation (k):

$$\frac{\partial}{\partial t}(\rho k)+\frac{\partial}{\partial x_j}(\rho k u_j)=\rho\tau_{ij}\frac{\partial u_i}{\partial x_j}-\rho\varepsilon-\gamma\rho\varepsilon M_T{}^2 +\frac{\partial}{\partial x_j}\left[\left(\mu+\frac{\mu_T}{\sigma_k}\right)\frac{\partial k}{\partial x_j}\right] \quad (3)$$

Dissipation rate equation (ε) :

$$\frac{\partial}{\partial t}(\rho\varepsilon)+\frac{\partial}{\partial x_j}(\rho\varepsilon u_j)=C_{\varepsilon 1}\frac{\varepsilon}{k}\rho\tau_{ij}\frac{\partial u_i}{\partial x_j}-C_{\varepsilon 2}\rho\frac{\varepsilon^2}{k} +\frac{\partial}{\partial x_j}\left[\left(\mu+\frac{\mu_T}{\sigma_\varepsilon}\right)\frac{\partial\varepsilon}{\partial x_j}\right]$$

Where,

$$\mu_T=C_\varepsilon\frac{\rho k^2}{\varepsilon},\quad C_\mu=0.09,\quad C_{\varepsilon 1}=1.44$$

$$C_{\varepsilon 2}=1.92,\quad \sigma_k=1.0,\quad \sigma_\varepsilon=1.3$$

Additionally, the shear stress and heat flux terms are calculated as,

$$\tau_{ij}=(\mu+\mu_T)\left[\left(\frac{\partial u_i}{\partial x_j}+\frac{\partial u_j}{\partial x_i}\right)-\frac{2}{3}\delta_{ij}\left(\frac{\partial u_m}{\partial x_m}\right)\right]-\frac{2}{3}\rho k\delta_{ij}$$

$$q_i=\left[\frac{\mu}{Pr_L}\frac{\partial T}{\partial x_i}+\frac{\mu_T}{Pr_T}\frac{\partial T}{\partial x_i}\right]$$

Launder and Spalding (1974) proposed a wall function for $k-\varepsilon$ model, and the same is used for the present study. It avoids the necessity to integrate the governing equations right to the wall to obey the universal behaviour of the near-wall flow. In the case of $k-\omega$ model, the present study utilizes the wall function proposed by Wilcox (1988). Also, an additional term M_T is considered to incorporate the compressibility correction (Sarkar *et al.* 1991). Figure 2 (a) represents the layer within the logarithmic region. The height of this region is defined by the point where turbulence production is equal to the dissipation rate. On the other side, in the absence of the wall function approach $k-\omega$ model requires a very stringent y^+ requirement as represented in Fig. 2 (b). Therefore the following wall functions are employed in the present solver.

$$k_p=\frac{u_\tau^2}{\sqrt{C_\mu}},\qquad \varepsilon_p=\frac{u_\tau^3}{\kappa y_p}$$

$$\omega_p=\frac{u_\tau}{\sqrt{C_\mu}\kappa y_p},\qquad 30<y_p^+<500$$

Where $C_\mu=0.09$ and $\kappa=0.41$

2.1. Computational Method

Solver employs a cell-centered, face-based algorithm to avoid repeated calculation of face fluxes; thus ensures reduced computational time. The popular advection upstream splitting method (AUSM scheme) Liou and Steffen Jr (1993) is employed to calculate the inviscid fluxes.} Whereas, the viscous fluxes are computed by using the gradients evaluated at the face centroids. Green-Gauss approach is followed to first evaluate the gradients at the cell centroids. Further, the computed cell centroid gradients are transferred to the faces and are used for the calculation of fluxes. A piecewise linear

reconstruction along with Venkatakrishnan limiter (Venkatakrishnan (1993)) is employed to achieve second-order spatial accuracy. The governing equations are integrated over the control volume and represented as

$$\int_{\Omega}\left(\frac{\partial U}{\partial t}+\frac{\partial}{\partial x}\left(F_I-F_V\right)+\frac{\partial}{\partial y}\left(G_I-G_V\right)\right)d\Omega=0$$

$$H_I=[F_I \quad G_I], H_V=[F_V \quad G_V], H=H_I-H_V$$

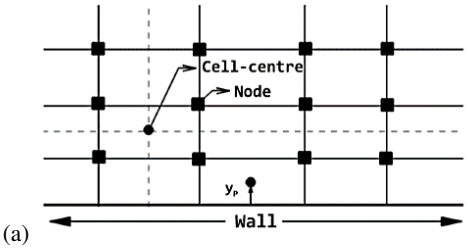

(a)

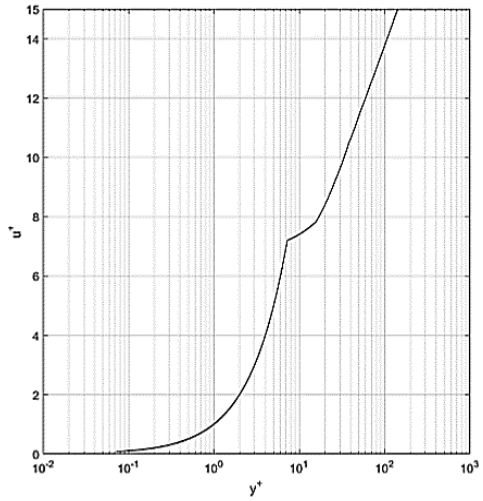

(b)

Fig. 2. (a) Wall function approach (b) u^+ vs y^+ graph plotted at the location of the start of interaction for $k-\omega$ model.

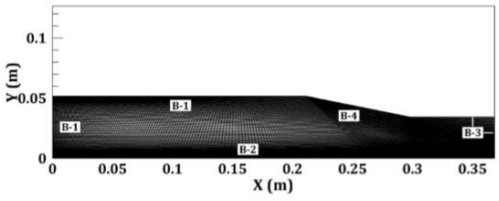

(a)

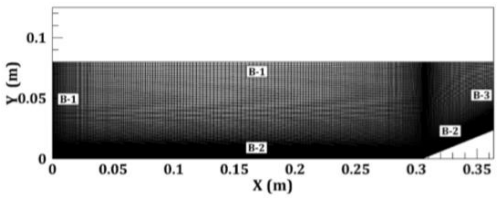

(b)

Fig. 3. Computational domain for (a) Shock-generator with an angle of 11.31^0 (b) Ramp with an angle of 23^0.

After applying Gauss Divergence theorem the above equation is written as

$$\vec{U}_i^{n+1}=\vec{U}_i^n-\frac{\Delta t}{\Omega_k}\left[\sum_{i=1}^{N}\vec{H}_{\perp}.\Delta S_i\right]_k$$

Where U is the Conservative vector F_I , G_I are convective fluxes and F_V , G_V are viscous fluxes. N is the total number of faces, Ω_k is the volume of the k^{th} cell, $H_{\perp i}$ is the total flux normal to the surface(ΔS_i) of k^{th} cell.

2.2. Computational Domain and Mesh

The present study aims on the comparison of two modes of shock-wave/boundary- layer interactions. In this study, the flowfield is considered as two dimensional and therefore the computational domains are taken as 2D domains. Further, the domains are meshed with quadrilateral elements by giving suitable refinement at key locations. Thus created sample computational domains for both I-SWBLI and R-SWBLI are depicted in Fig.3(a) and (b) respectively.

In the case of supersonic flow, the grid refinement can influence the numerical prediction of shock waves and the boundary layer. For instance, the first layer height near the wall boundary of the domain needs to be chosen so as to ensure y^+ value within the acceptable limit of turbulence model employed in the simulation. Hence a suitable near wall refinement has been carried out during the grid generation phase to ensure the earlier mentioned y^+ requirement. Optimally refined grid had a first layer height of the order of 3×10^{-5} m, which ensured y^+ values close to 30 for simulations employing wall functions.} Upon considering the primary focus of the present study as the exploration of SWBLI equivalence, various ramp angles and their corresponding shock generator angles that result in the same pressure rise as reported in the experimental studies of Law (1976) are chosen for the investigation. Thus, chosen ramp and shock generator angles are tabulated in Table 1. The computational domains considered for the present study have four boundary conditions. They are supersonic inlet, inviscid wall, viscous wall and supersonic outlet. The notations for the boundary conditions are shown in Table 2. The freestream conditions employed in the present study are adapted from the tunnel conditions of Law's experimental work Law (1976). The freestream Mach number, pressure, temperature are maintained as 2.96, 10963 Pa and 98.9K respectively. The corresponding Reynolds number based on the boundary layer thickness at beginning of interaction is 1.5×10^5 . Therefore, the inlet boundary has been assigned with these freestream conditions. Whereas, the outlet has been taken as supersonic outlet and the flow variables have been extrapolated from the corresponding neighbour cells. The viscous wall boundaries have been set with no-slip, adiabatic conditions.

Table 1 Ramp and its corresponding shock generator angle in deg

Ramp (α_R)	Shock generator (α_{SG})
22	10.83
23	11.31
24	11.79
25	12.27

Table 2 List of boundary conditions used for the computational study

Notations	Boundary conditions
B-1	Supersonic inlet
B-2	Viscous wall
B-3	Supersonic outlet
B-4	Inviscid wall

To minimize the grid-resulted error in the final solution, a thorough grid independence study has been carried out for each test cases. Each computational domain has been finalized after a series of grid independence study. Sample grid independence studies performed for R-SWBLI case with $\alpha_R = 22^0$ and I-SWBLI case with $\alpha_{SG} = 10.83^0$ are presented in Fig.4 (a) and (b) respectively. It can be noted from these figures that the coarse grids do not predict the separation bubble accurately. However, the subsequent refinement of the grid ensured the numerical prediction closer to the experimental measurement. A slight dip in the pressure measurements recorded at the pre-interaction region of I-SWBLI case, as evident in Fig. 4 (b) might be interpreted as negligible measurement error of experiment. However, besides the very good agreement of experimental and numerical results in most of the regions, the post-interaction region of I-SWBLI case showed slight mismatch when employing the $k-\varepsilon$ model. This disparity may be of turbulence model specific. In the case of $k-\varepsilon$ model, further refinement of the grid by increasing the number of nodes has not resulted in any substantial changes in the numerical solution. So, a medium level grid with 320×120 nodes in case of ramp and 320×80 nodes in case of shock generator is sufficient to accurately resolve the flow-field. These converged grids have wall y^+ in the range of $30-40$. The fine grids having a higher number of nodes did not offer significant changes in the solution but consumed more computational time. Thus, medium grids are used for the simulations. It is to be noted that the grid independent domain of $k-\varepsilon$ model may not be a grid-independent domain for $k-\omega$ model. Hence separate grid-independence studies have been carried out by considering different turbulence models and varieties of geometries. The steady-state solutions obtained on such grid independent computational domains are employed for presenting the results and discussions.

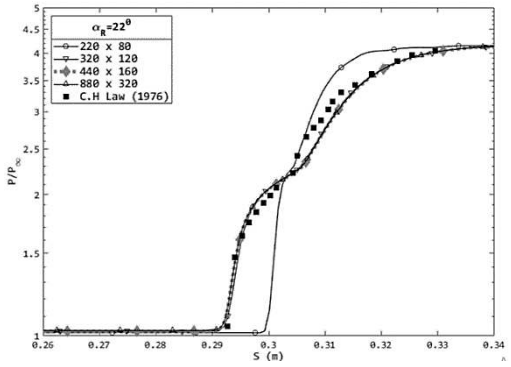

(a)

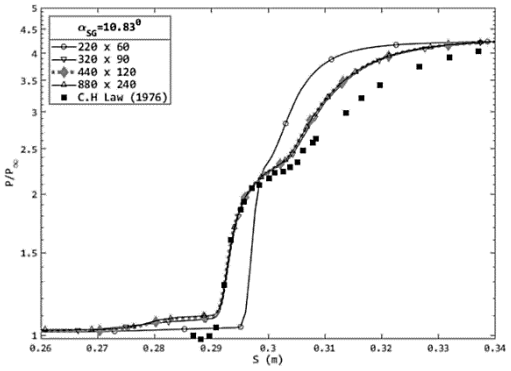

(b)

Fig. 4. Grid independence study.

3. RESULTS

In the present study, the flow separation due to I-SWBLI and R-SWBLI are investigated. Generally, the characteristics of SWBLI induced separation bubble depends on freestream Mach number, Reynolds number and geometrical parameters of the source of shock generation. The increment in shock strength results in immediate thickening of the subsonic region at the point of SWBLI. So the adverse pressure gradient effect will start to propagate upstream of the interaction region through this subsonic boundary layer. Once the combined effect of adverse pressure gradient and wall friction dominates over the inertia, the flow will separate abruptly. The separated flow then behaves like a free shear layer inside the zone of separation. Further, due to mixing the kinetic energy of the reversed flow may increase. Later it helps to overcome the adverse pressure gradient at the point of reattachment Viswanath (1988).

The numerical schlieren images obtained for two different SWBLI cases of same overall pressure rise are depicted in Fig. 5. Here in Fig.5 (a), a compression corner of 25^0 deflection angle is responsible for the SWBLI. As mentioned before, the presence of compression corner forces the supersonic flow to deflect by 25^0. Such abrupt flow deflection creates thickening of the subsonic boundary layer on the wall. The upstream disturbance and associated thickening of the subsonic part of the boundary layer lead to the

deflection of supersonic flow above it. When the adverse pressure gradient induced by the ramp exceeds the incipient separation condition, boundary layer flow eventually separates. The number of weak compression waves created as a result of local supersonic flow deflection coalesce to form a strong separation shock at the separation point. The separated shear layer further reattaches on the ramp surface as a result of kinetic energy gained from the upper decks. The reattachment occurs by passing across another compression wave named as reattachment shock. A recirculation zone, bounded by the separation and reattachment shocks forms, as shown in Fig. 5 (a). A triple point also gets, formed due to the interaction of separation and reattachment shocks. The reattached flow may continue as wall bounded flow until it experiences an additional adverse pressure gradient situation.

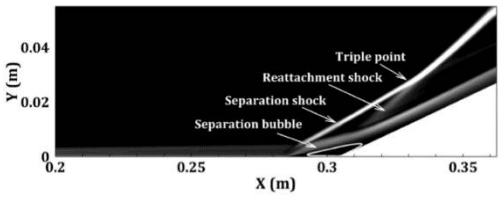

(a)

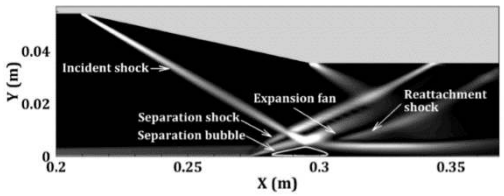

(b)

Fig. 5. Numerical schlieren image for (a) compression ramp with 25^0 (b)shock generator with $12{:}27^0$

Examination of flow structure associated with I-SWBLI (see Fig.5(b)) shows that the flow separation persists in this case as well. Unlike the previous case of R-SWBLI, here, the adverse pressure gradient is induced by a shock that is impinging on the boundary layer. However, the boundary layer responds to the shock-induced pressure gradient very identical to that of R-SWBLI case. The upstream disturbance propagation, boundary layer thickening and eventual separation of the flow are observed in the I-SWBLI case too. Hence one can observe that the separation dynamics of R-SWBLI and I-SWBLI are the same. However, the I-SWBLI has some notable difference in the flow structure. The main difference of I-SWBLI flow structure in the occurrence of an additional expansion fan from the interaction location. Therefore, the separated flow undergoes a gradual turning across the expansion fan followed by a sharp turning across another compression wave before the reattachment. In spite of these differences in inviscid flow aspects, the flow separation characteristics of R-SWBLI and I-SWBLI are noted to be the same when maintained same overall pressure rise in both the cases. In order to have the same overall pressure rise in both the cases, it is essential to maintain the same overall flow deflection for both I-SWBLI flow field and R-SWBLI flow field. That means the ramp angle must be close to double the value shock generator angle.

The surface pressure distributions on the R-SWBLI and I-SWBLI models are compared in Fig.6. It is evident from the figure that the pressure distributions of R-SWBLI case with $\alpha_R = 25^0$ and I-SWBLI case with $\alpha_{SG} = 12.27^0$ are closely matching. The same observations can be made from the pressure distributions of other R-SWBLI and I-SWBLI combinations as well. For all the pressure distribution curves presented in Fig. 6, there are three notable inflection points. The first inflection point belongs to upstream influence extent point, whereas the second and third are corresponding to separation and reattachment points respectively. Further, the locations of these three inflection points are different for various equivalent flow deflection angles (α_{equ}). This observation speaks about the dependency of upstream influence and flow separation on the flow deflection angle. However, they are independent of the mode of SWBLI. For instance, all three inflection locations are almost the same for the cases of both $\alpha_R = 25^0$ and $\alpha_{SG} = 12.27^0$. This again supports the equivalence of two different modes of SWBLI.

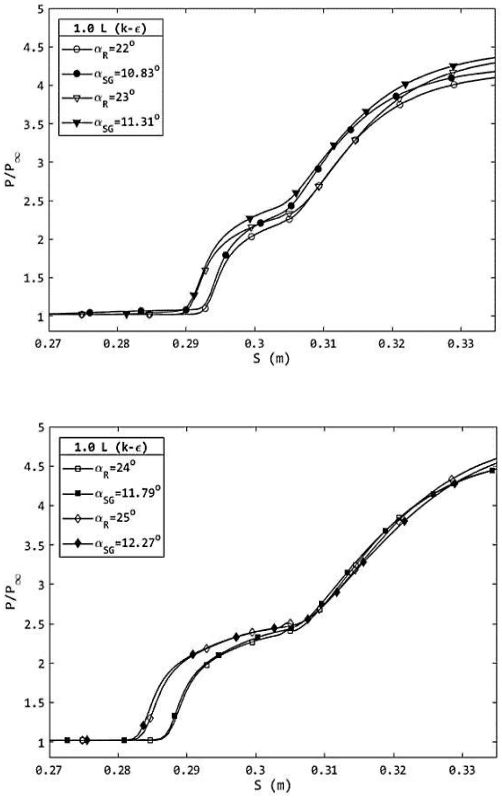

Fig. 6. Comparison of surface pressure distribution on the ramp and its equivalent shock generator at the 1.0L case.

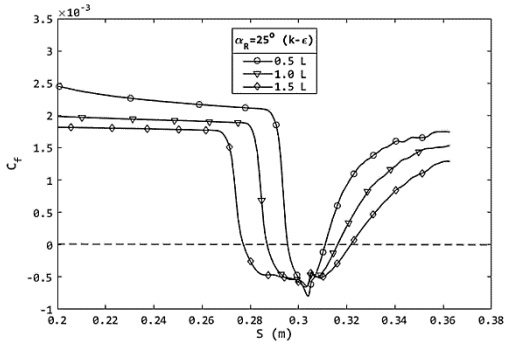

Fig. 7. Skin friction coefficient distribution considered for the measurement of separation bubble size.

Further to analyse and compare the sizes of separation bubble/length of the separated region obtained with I-SWBLI and R-SWBLI cases, the shear stress distributions obtained on the surface of the models are considered. The comparison of non-dimensional surface-shear stress (skin friction coefficient) distributions of R-SWBLI is presented in Fig.7. The separation bubble size can be measured from Fig.7 as the surface length between the first and second zero-shear stress points. The shear stress remains negative within the separation zone. Thus, measured separation bubble sizes (L_b) of different ramp and impingement cases are presented in Fig.8. It is clearly evident from Fig.8 that the separation bubble sizes of ramp and the equivalent shock impingement case are very close. There is almost 1 mm difference between the separation bubble sizes of R-SWBLI and I-SWBLI for the cases of all flow deflection angles. It is to be attributed to the fact that the α_{SG} values are not precisely half of their equivalent ramp angle α_R . For instance for ramp angle of $\alpha_R = 25^0$, the equivalent shock generator angle was 12.27^0 not 12.5^0 . This deviation has been purposefully retained in the present simulations to ensure one to one comparison of numerical and experimental measurements.

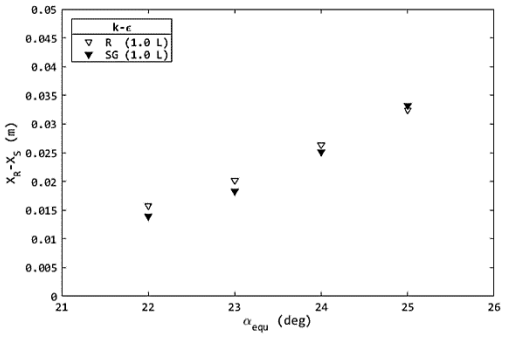

Fig. 8. Comparison of separation bubble size obtained for different I-SWBLI and R-SWBLI cases.

On identifying the equivalence of two different modes of SWBLI, it is important to revisit the flow-field to understand the underlying flow physics leading to this equivalence. It is a known fact that the separation bubble created in case of SWBLI mainly depends on the nature and properties of approaching boundary layer, freestream Mach number and the total flow deflection induced by the ramp/impinging shock. In the present case, while considering a particular ramp angle (α_R) and its equivalent shock generator angle (α_{SG}) the previously mentioned parameters are common, but the inviscid flow structures of SWBLI are different. However, the observed equivalence speaks that the separation dynamics depends on boundary layer aspects alone not on the inviscid flow structure. To ascertain this fact the boundary layer velocity profiles have been analyzed at various flat plate locations. Figure 9 shows the non-dimensional velocity distribution normal to the flat plate plotted at a point far upstream of the interaction location, boundary layer separation point, origin of the separation bubble and at the point of reattachment. The boundary layer profiles depicted in Fig. 9 clearly indicate that the boundary layer development on the flat plate section of the models is the same. The close match of velocity profiles well upstream of the interaction location is a quite obvious observation, as the approaching freestream is same for both I-SWBLI and R-SWBLI cases. However, it is important to note the impact of flow deflector on the velocity profiles within the interaction zone. Surprisingly, the velocity profiles of I-SWBLI and R-SWBLI cases are the same at the point of separation, within the separation and even at reattachment point. This observation points towards the fact that, regardless of the means of adverse pressure gradient imposed to the boundary layer, those pressure disturbances propagate and influence the boundary layer in a similar fashion. Current observations are in consonance with free interaction theory. According to free interaction theory, the pressure rise on separation and plateau-pressure are independent of the mode of interaction, hence the nature of separation region too.

Further, to demonstrate the difference in flow structure just above the boundary layer region, the Mach number variation along the flow direction is considered at a location $y = 9mm$ from the wall and that is presented in Fig.10. There are two locations on the Mach number distribution of R-SWBLI where the Mach number drops. Those are the locations at which flow encounter the shocks. The first Mach number drop is because of separation shock, whereas the second one is due to the reattachment shock. Apart from the two Mach jumps there are no other abrupt changes in the distribution for R-SWBLI case. On the other hand, In the case of I-SWBLI, one can notice more discontinuities/changes. The first drop in the Mach number happens again across separation shock of I-SWBLI case. Just after the Mach number drop, there is a visible gradual rise in Mach number. This is because of the expansion fan originated from the interaction location. After this, the Mach number again starts to decrease across the reattachment shock. After reattachment shock, the Mach number begins to increase due to presents of expansion waves. Hence the Mach number distributions

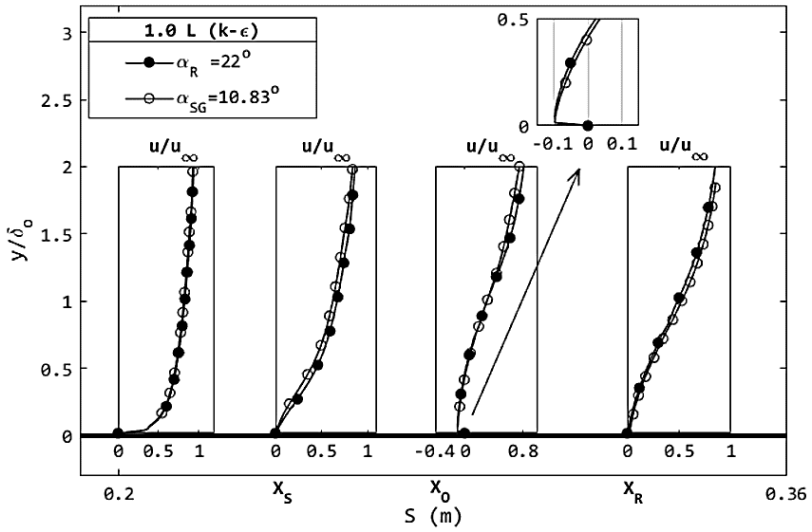

Fig. 9. Boundary layer profiles at various locations over the flat plate section of SWBLI geometries.

compared in Fig.10 clearly show the disparities of I-SWBLI and R-SWBLI flow structure. Since there are considerable differences in the flow just above the boundary layer, one can expect notable differences in the boundary phenomenon as well, especially in the core regions of the interactions. However, the boundary layer profiles plotted at the separation point, the origin of interaction and reattachment point are not showing any notable difference between two SWBLI cases. These considerations suggest that the momentum energy exchange from the upper supersonic deck to the lower subsonic deck of the SWBLI is not significant. It is essentially the adverse pressure gradient induced by the impinging shock or ramp is responsible for the separation structure and the extent of separation. As long as the overall adverse pressure gradient is the same, the SWBLI induced flow separation remain the same irrespective of the mode of interaction.

3.1 Comparative Accuracy of Turbulence Models in the Prediction of SWBLI

For the present study, two different two-equation turbulence models were incorporated into the in-house solver, viz. the $k-\omega$ model and the $k-\varepsilon$ model. The main difference of $k-\varepsilon$ model from $k-\omega$ model is the necessity of implementing a suitable wall function to accurately predict near wall turbulence induced by the wall. However, the $k-\omega$ model doesn't require wall function, but its accuracy would largely depend on the first layer height and associated y^+ value. In the current study, the wall function proposed by Launder and Spalding (1974) has been employed for the $k-\varepsilon$ formulation, whereas for the case of $k-\omega$ model, the first layer height near the wall has to be set in such a way that wall y^+ remains lesser than unity. The very strict y^+ requirement of $k-\omega$ model lead to increase of computational time. To reduce this, a wall function proposed by Wilcox (1988) was employed for the present work. On the other hand, the less stringent nature of $k-\varepsilon$ model's y^+ requirements allowed the authors to use bit more coarser mesh near the wall region and thus reduced the simulation time.

The simulations of all ramp and shock generator cases were carried out using both the turbulence models. To assess the prediction accuracy of these models, numerical results are further compared with experimental measurements. Law (1976) had measured the surface pressure distributions on all the test geometries during the original experimental study. Thus the experimental surface pressure data can be effectively used to verify the computational results. Additionally, the experimentally calculated separation bubble sizes are also compared with numerically predicted separation bubble sizes. Figure 11 depicts the surface pressure variation along the wall of 22^0 ramp angle case. The surface pressure distributions of an equivalent shock generator case ($\alpha_{SG}=10.83^0$) is presented in Fig. 12. It is clearly evident from the Fig. 11 and 12 that the numerical predictions are of comparable accuracy to that of experimental measurements.

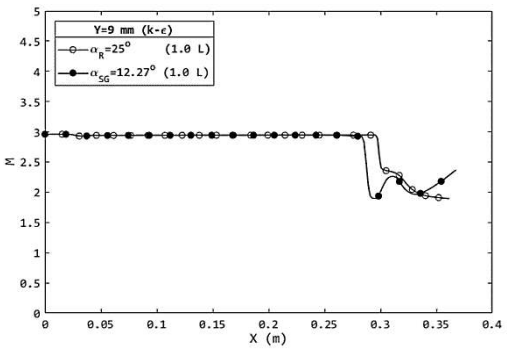

Fig. 10. Mach number variation along the flow direction.

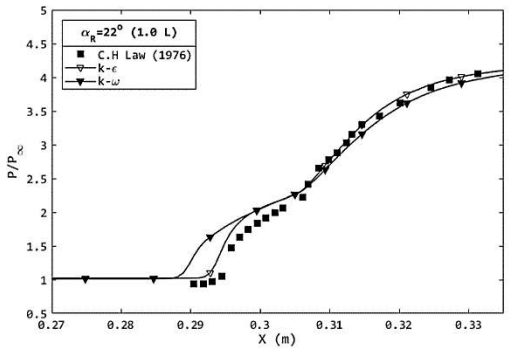

Fig. 11. Surface pressure comparison of ramp case with an angle of 22^0.

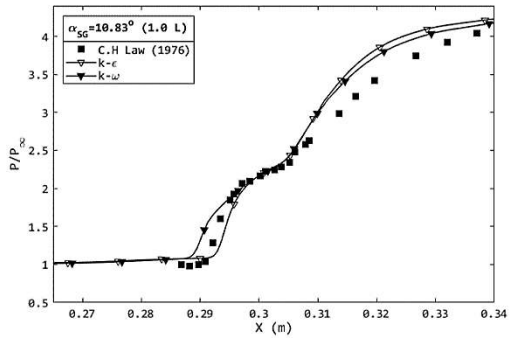

Fig. 12. Surface pressure comparison of the shock generator case with an angle of $10:83^0$.

Surprisingly the distributions obtained with $k-\varepsilon$ model is showing a high level of agreement with the experiment upstream of the reattachment point. The upstream influence location, the point at which the pressure distribution of undisturbed boundary layer starts deviating, predicted by $k-\varepsilon$ model is exactly the same as that of experimental prediction. On the other hand, $k-\omega$ model over predicts the upstream influence length (the axial distance between the hinge location and upstream influence point). However, the pressure distributions at the post reattachment location obtained with both the models are almost the same and are in reasonable agreement with experimental measurements.

Subsequently the surface shear stress predicted by different models have been analyzed and separation bubble sizes have been evaluated by following the methodology mentioned earlier. Two different parameters of separation bubble are considered for the analysis. The first one is the axial distance between the point of separation (X_s) and the origin of interaction (X_o). The second parameter considered for the comparison is the separation bubble size (L_b) itself. The half separation bubble size (X_o - X_s) obtained from the simulations are compared with experimental measurements in Fig. 13. It is very evident from Fig. 13 (a) and (b) that the numerical predictions of present $k-\varepsilon$ model are reasonably matching with experimental measurements. However, the $k-\omega$ solver over predicts the half size of the separation bubble in all the cases. Further, the separation bubble sizes predicted by both the models are compared in Fig.14. Here this comparison is aimed to explore the accuracy of turbulence model in precisely predicting the full separation bubble size, both in the case of I-SWBLI and R-SWBLI. It is also important to identify which scheme would predict the SWBLI equivalence better. A close analysis of Fig. 14 indicates that the SWBLI-equivalence is better predicted by the $k-\varepsilon$ model. However, the predictions are very consistent in case of $k-\omega$ model. That means, in the case of $k-\omega$ model, the separation bubble size of ramp is always higher than that of shock generator for all the equivalent flow deflection cases. Where as in the case of $k-\varepsilon$ model, although predicted separation bubble sizes are slightly lesser than that of $k-\omega$ model, the consistency in the prediction couldn't be observed. At lower flow deflection angles, ramp cases have slightly higher (X_o - X_s). But at higher deflection angle case, for instance in the case of $\alpha_{equ} = 25^0$, the shock generator has a slightly higher separation bubble size as compared to it's equivalent ramp case. In spite of this, the overall performance of present $k-\varepsilon$ model with improved wall function is comparatively better than the $k-\omega$ model. Another important fact to note from Fig. 14 is that the experimentally obtained (X_o - X_s) are comparatively lesser than that of numerical predictions. This can be attributed to the disparity in methodologies followed for the identification of separation location.

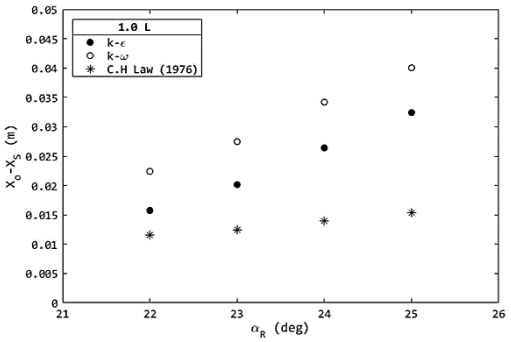

(a)

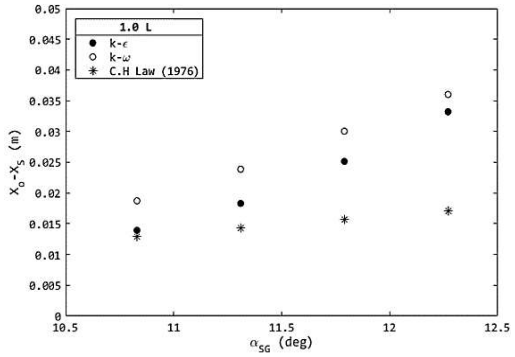

(b)

Fig. 13. comparison of (Xo -Xs) obtained with different turbulence models (a) R-SWBLI case and (b) I-SWBLI case.

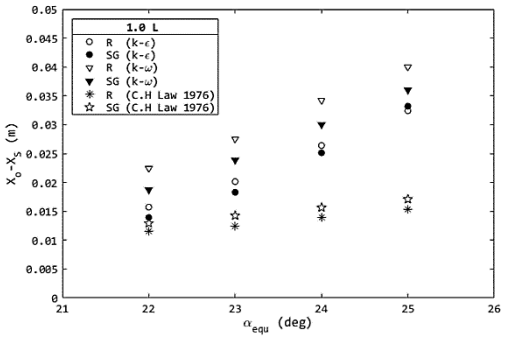

Fig. 14. comparison of (Xo -Xs) obtained with different turbulence models.

3.2. Effect of Undisturbed Boundary Layer Thickness on the SWBL- Induced Flow Separation

It is important to identify the effects of simultaneous change in ramp/shock generator angle and the thickness of the undisturbed boundary layer on the separation bubble size. In the present study, to realize the variation in boundary layer thickness, the length of the flat plate section of SWBLI geometries has been changed. Three different variants of the flat plate have been employed for the study, viz., 0.5L, 1.0L and 1.5L. Where L is the length of the original flat plate considered in the experimental studies of Law (1976). The surface pressure distribution obtained for a representative shock generator case is presented in Fig. 15. Three different flat plate length cases are compared in this figure. It is evident that the location of the upstream influence shifts further and further upstream when the flat plate length increases. For the same freestream conditions, increase in flat plate length leads to an increase in boundary layer thickness. According to the Blasius solution, the boundary layer thickness ` δ ' can be correlated as $\delta \propto x^{\frac{4}{5}}$. The higher the boundary layer thickness, the thicker the subsonic part of it. Hence, through such thicker subsonic part, more upstream propagation of pressure disturbance is possible. This is very evident in Fig. 15. The most upstream surface pressure deviation can be noted in the case of 1.5L. The upstream influence location/beginning of interaction is the location at which the usual flat plate pressure distribution start rising due to the effect of downstream ramp/impingement shock. The least upstream influence extent is noticed in the case of a flat plate with 0.5L length. Additionally, the size of the plateau pressure region in the distribution also noticed to be increasing with an increase in flat plate length.

The dimensional separation bubble size ($X_R - X_S$) obtained for all the cases of flow deflection angles is plotted in Fig. 16. A linear increase in separation bubble size with increase equivalent flow deflection angle (α_{equ}) can be noted for all the flat plate cases. The slope of the separation bubble trend is maximum in case of longest flat plate and a relatively smaller slope recorded for shorter flat plate case. This observation implies that the separation bubble is a function of both total flow deflection angle and undisturbed boundary layer thickness. The observed difference in slopes gives an impression that at some lower flow deflection angle, all three flat plate cases may provide the same separation bubble size. Since the separation of flow necessitates a critical flow deflection angle, termed as incipient separation angle, the above-stated condition may not be correct. According to Needham and Stollery (Needham and Stollery 1966), the incipient separation angle is defined as,

$$\theta_{is} = \frac{80\sqrt{\overline{\chi_L}}}{M_\infty} \tag{5}$$

where χ_L is the viscous interaction parameter at the flat plate-ramp junction, and is given by,

$$\overline{\chi_L} = M_\infty^3 \sqrt{C} / \sqrt{Re_L} \tag{6}$$

Where,

$$C = \frac{\mu_W T_\infty}{\mu_\infty T_W} \tag{7}$$

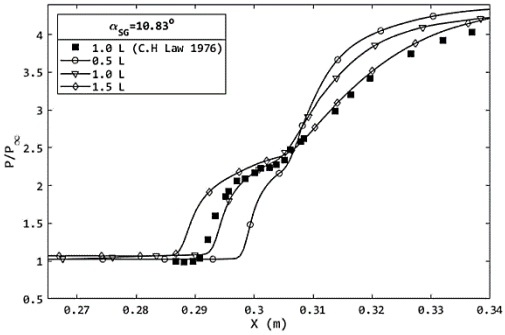

Fig. 15. Comparison of surface pressure distributions Obtained with different flat plate cases.

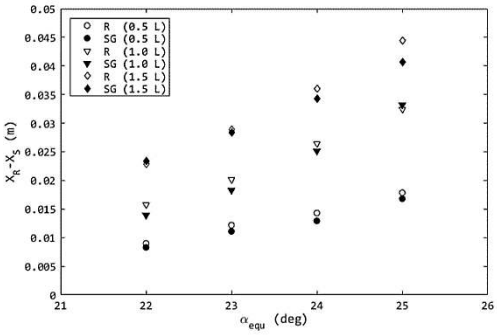

Fig. 16. Comparison of separation bubble sizes obtained with different flat plate and flow deflection angle combinations.

If the deflection angle is higher than the incipient separation angle, then boundary layer separation takes place. It is clear from the above equations that, for longer flat plate the Re_L would be higher and θ_{is} would be lesser. Hence the trend lines of different flat plate cases do not meet. That means, in reality

there will be no condition at which boundary layers of different thicknesses encounter the same flow deflector of prefixed deflection angle and give same separation bubble sizes. Figure 16 once again confirms the equivalence of I-SWBLI and R-SWBLI. The separation bubble sizes obtained with different means of SWBLI are the same, even for different approaching boundary layer conditions. Hence for a given freestream and same undisturbed boundary layer conditions the flow separation induced by both I-SWBLI and R-SWBLI remain the same. All the pairs of data points presented in Fig. 16 satisfy the above-stated fact. There is only a minor deviation for the combination of α_{equ} of 25^0 and flat plate length of 1.5L. Further to analyse the effect of boundary layer thickness and flow deflection angle on the upstream part of the separation bubble/half separation size, the distance between the hinge location and the separation point ($X_0 - X_S$) has been measured for all the tested cases. Thus obtained data points for the ramp cases are plotted in Fig. 17. The trend of half separation size is very similar to that observed in the case of separation bubble size.

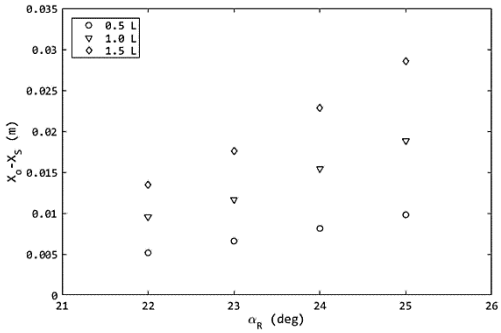

Fig. 17. Comparison of half separation bubble sizes obtained with different flat plate and ramp angle combinations.

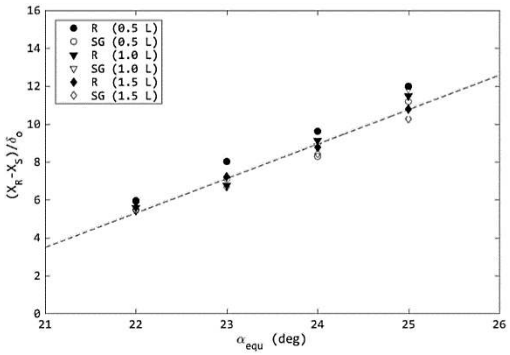

Fig. 18. Comparison of scaled separation bubble sizes.

So the analysis shows that the separation bubble size and half separation size are functions of deflection angle and boundary layer thickness. Also, it is explored that the separation bubble size increases almost linearly with an increase in boundary layer thickness. So, the length of the separated region and $X_0 - X_s$ are further scaled with δ_o , and are plotted in Fig. 18 and 19 respectively. In Fig. 19, in addition to the numerical predictions, experimental data points are also plotted. It is very evident from the figure that, when presented in non-dimensional form the separation bubble sizes of different flat plate cases almost fall into a single trend line. The same observation can be made from the plot of $X_0 - X_s$ as well. The experimentally predicted data points are slightly off-trend, mainly because of the disparity in the separation bubble calculation methodology followed in the experiment and numerical study. In addition to that, the present simulations are purely two dimensional studies, hence the probable 3D effects that were involved in the actual experiments are not taken cared. However the comparison of pressure distributions presented earlier support the overall two dimensional nature of the interactions. In addition to that, the observed differences of separation bubble sizes are within the acceptable limit even for the cases of high equivalent flow deflection angles.

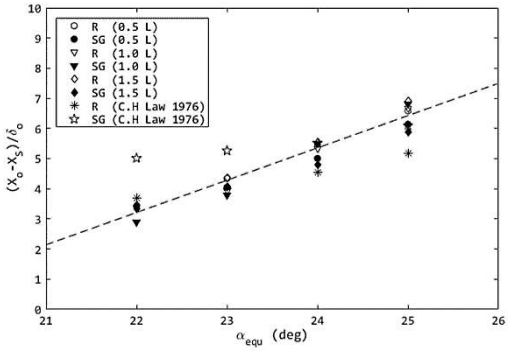

Fig. 19. Comparison of scaled $X_0 - X_s$.

Table 3 Details of additional cases considered

Add. case 1& 2 Schülein (2006) $\alpha_{SG} = 14^0$ (case 1) $\alpha_R = 10^0$ (case 2)	M_∞=5.0 $Re\infty = 3.7\times107m{-}1$ $P_0 = 21.2bar$ $T_0 = 410K\ \delta_0 = 4.77mm$
Add. case 3 Borovoi *et al*. (2011) $\alpha SG = 15^0$	M_∞=5.0 $Re_\infty = 8.46\times10^7 m^{-1}$ $P_0 = 70bar\ T_0 = 510K\ \delta_0 = 2.88mm$
Add. case 4 Settles (1976) $\alpha_R = 24^0$	M_∞=2.85 $Re\infty = 6.3\times107m{-}1$ $P_0 = 6.89bar\ T_0 = 262.2K\ \delta_0 = 21mm$

Additional numerical simulations have been undertaken by employing four more experimental conditions to ascertain the identified equivalence of two modes of interactions. Details of these SWBLI

test cases are summarized in table 3. These listed experiments were focusing either on I-SWBLI or R-SWBLI. Comparison of two types of interaction was not in the scope of those studies. However, to prove the equivalence, simulations are repeated with $k-\varepsilon$ solver for both types of interactions by constructing suitable computational domains. Thus predicted surface pressure distributions of "Add. case 1" are compared with experimental measurements in Fig. 20. Numerical predictions are in close agreement with experimental data and the distributions of I-SWBLI and R-SWBLI are very identical. The comparison of length of the separated regions obtained for above mentioned additional cases scaled with respective boundary layer thickness values (δ_o) is presented in Fig. 21. It can be noted that the equivalence of two modes of interaction remains valid for diverse freestream conditions as long as the same overall pressure rise across the interaction zone is maintained in both the cases.

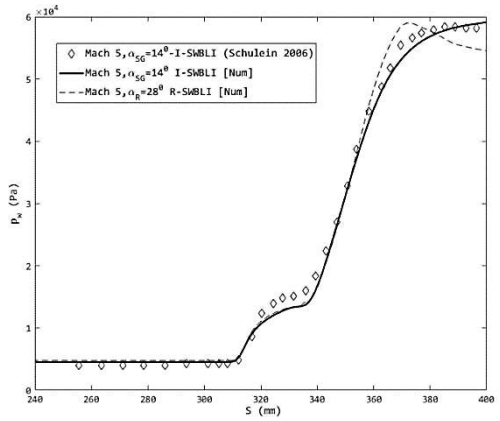

Fig. 20. Comparison of surface pressure distributions of Add. case 1.

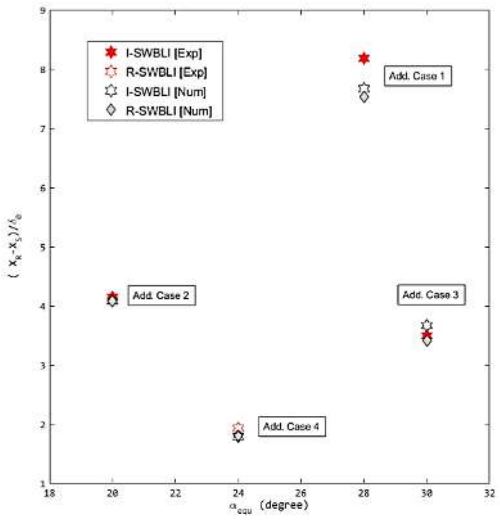

Fig. 21. Comparison of scaled length of separated regions of additional cases.

4. CONCLUSION

The equivalence of shock wave boundary layer interactions induced by two different modes, viz. impinging shock-induced and ramp induced have been investigated. An in-house developed, higher-order accurate, compressible, turbulent flow solver was used for this numerical study. The computed surface pressure distributions and separation bubble sizes are noted to be in good agreement with the experimental measurements. For the given freestream condition, the SWBLI-induced separation bubble size noted to be varying with the change in equivalent flow deflection angle. For the same overall pressure rise, the R-SWBLI and the I-SWBLI have produced nearly equal separation bubble sizes. The half separation bubble sizes were also noted to be the same for both kinds of SWBLIs at that condition. Additional SWBLI cases with different freestream conditions were also studied to ascertain this equivalence criteria. Both $k-\omega$ and $k-\grave{o}$ turbulence models have been employed in this study. The $k-\omega$ model slightly over predicted the separation bubble size in comparison to experimental measurements. The $k-\varepsilon$ model with the enhanced wall function of present solver predicted the SWBLI parameters with improved accuracy and with good agreement to the experimental measurements. The absolute values of separation bubble size and half separation size are functions of overall flow deflection angle and thickness of the undisturbed boundary layer at the beginning of the interaction. However, the scaled separation bubble sizes observed to be falling into a single linear trend when the undisturbed boundary layer thickness at the beginning of the interaction is used as the scaling parameter. The plateau pressure was identified as a free interaction parameter that doesn't depend on the flow deflection angle and the Reynolds number at the origin of interaction. The SWBLI-equivalence is identified as independent of local Reynolds number. Hence, authors are on the opinion that the R-SWBLI and I-SWBLI can be interchanged to address various design constraints of aerospace systems.

ACKNOWLEDGEMENTS

This research was supported by Science and Engineering Research Board (SERB), Government of India through the early career research grant (ECR/2016/001873) issued to the first author.

REFERENCES

Aubard, G., X. Gloerfelt and J. C. Robinet (2013). Large-eddy simulation of broadband unsteadiness in a shock/boundary-layer interaction. *AIAA Journal* 51(10), 2395–2409.

Babinsky, H. and H. Ogawa (2008). Sbli control for wings and inlets. *Shock Waves* 18(2), 89.

Babinsky, H. and J. K. Harvey(2011). *Shock wave-boundary-layer interactions*, Volume 32. Cambridge University Press.

Bodonyi, R. J. and F. T. Smith (1986). Shockwave laminar boundary-layer interaction in supercritical transonic flow. *Computers &*

Fluids 14(2), 97–108.

Borovoi, V. Y., I. Egorov, A. Y. Noev, A. Skuratov and I. Struminskaya (2011). Twodimensional interaction between an incident shock and a turbulent boundary layer in the presence of an entropy layer. *Fluid Dynamics* 46(6), 917–934.

Catalano, P. and M. Amato (2003). An evaluation of rans turbulence modelling for aerodynamic applications. *Aerospace Science and Technology* 7(7), 493–509.

Celik, I. (2005). RANS/LES/DES/DNS: the future prospects of turbulence modeling. *Journal of Fluids Engineering* 127(5), 829–830.

Chapman, D. R., D. M. Kuehn and H. K. Larson (1958). Investigation of separated flows in supersonic and subsonic streams with emphasis on the effect of transition. *NACA Rep.*, 1356.

Christopher, J. R. and G. B. Frederick (2006). Review and assessment of turbulence models for hypersonic flows. *Progress in Aerospace Sciences* 42(7–8), 469–530.

Davis, J. P. and B. Sturtevant (2000). Separation length in high-enthalpy shock/boundarylayer interaction. *Physics of Fluids* 12(10), 2661–2687.

Degrez, G., C. H. Boccadoro and J. F. Wendt (1987). The interaction of an oblique shock wave with a laminar boundary layer revisited. an experimental and numerical study. *Journal of Fluid Mechanics* 177, 247–263.

Delery, J. M. (1985). Shock wave/turbulent boundary layer interaction and its control. *Progress in Aerospace Sciences* 22(4), 209–280.

Garnier, E., P. Sagaut and M. Deville (2002). Large eddy simulation of shock/boundary layer interaction. *AIAA Journal* 40(10), 1935–1944.

Grasso, F. and M. Marini (1996). Analysis of hypersonic shock-wave laminar boundarylayer interaction phenomena. *Computers & Fluids* 25(6), 561–581.

Holden, M. (1977). Shock wave-turbulent boundary layer interaction in hypersonic flow. In *15th Aerospace Sciences Meeting*, pp. 45.

John, B. and V. Kulkarni (2014). Numerical assessment of correlations for shock wave boundary layer interaction. *Computers & Fluids* 90, 42–50.

Katzer, E. (1989). On the lengthscales of laminar shock/boundary-layer interaction. *Journal of Fluid Mechanics* 206, 477–496.

Knight, D., H. Yan, A. G. Panaras and A. Zheltovodov (2003). Advances in cfd prediction of shock wave turbulent boundary layer interactions. *Progress in Aerospace Sciences* 39(2-3), 121–184.

Korkegi, R. H. (1971). Survey of viscous interactions associated with high mach number flight. *AIAA Journal* 9(5), 771–784.

Launder, B. E. and D. B. Spalding (1972). *Lectures in Mathematical Models of Turbulence*. Academic Press, London, England.

Launder, B. E. and D. B. Spalding (1974). The numerical computation of turbulent flows. *Computer Methods in Applied Mechanics and Engineering* 2(2), 269–289.

Law, C. H. (1976). Supersonic shock wave turbulent boundary-layer interactions. *AIAA Journal* 14(6), 730–734.

Liepmann, H. W. (1946). The interaction between boundary layer and shock waves in transonic flow. *Journal of the Aeronautical Sciences* 13(12), 623–637.

Liou, M. S. and C. J. Steffen Jr (1993). A new flux splitting scheme. *Journal of Computational physics* 107(1), 23–39.

Meneveau, C. and J. Katz (2000). Scaleinvariance and turbulence models for largeeddy simulation. *Annual Review of Fluid Mechanics* 32(1), 1–32.

Moin, P. and K. Mahesh (1998). Direct numerical simulation: a tool in turbulence research. *Annual Review of Fluid Mechanics* 30(1), 539–578.

Needham, D. and J. Stollery (1966). Boundary layer separation in hypersonic flow. In *3rd and 4th Aerospace Sciences Meeting*, pp. 455.

Nichols, J. W., J. Larsson, M. Bernardini and S. Pirozzoli (2017). Stability and modal analysis of shock/boundary layer interactions. *Theoretical and Computational Fluid Dynamics* 31(1), 33–50.

Pirozzoli, S. and F. Grasso (2006). Direct numerical simulation of impinging shock wave/turbulent boundary layer interaction at m= 2.25. *Physics of Fluids* 18(6), 065113.

Sarkar, S., G. Erlebacher, M. Y. Hussaini and H. O. Kreiss (1991). The analysis and modelling of dilatational terms in compressible turbulence. *Journal of Fluid Mechanics* 227, 473–493.

Schülein, E. (2006). Skin friction and heat flux¨ measurements in shock/boundary layer interaction flows. *AIAA Journal* 44(8), 1732– 1741.

Settles, G. S. (1976). An experimental study of compressible turbulent boundary layer separation at high Reynolds numbers. *PhDT*.

Sriram, R., L. Srinath, M. K. K. Devaraj and G. Jagadeesh (2016). On the length scales of

hypersonic shock-induced large separation bubbles near leading edges. *Journal of Fluid Mechanics* 806, 304–355.

Venkatakrishnan, V. (1993). On the accuracy of limiters and convergence to steady state solutions. In *31st Aerospace Sciences Meeting*, pp. 880.

Viswanath, P. (1988). Shock-wave-turbulentboundary-layer interaction and its control: A survey of recent developments. *Sadhana* 12(1-2), 45–104.

Wilcox, D. C. (1988). Reassessment of the scaledetermining equation for advanced turbulence models. *AIAA journal* 26(11), 1299– 1310.

Wilcox, D. C. (1998). *Turbulence modeling for CFD*, Volume 2. DCW industries La Canada, CA.

Zhang, Y., H. J. Tan, M. C. Du and D. P. Wang (2014). Control of shock/boundary-layer interaction for hypersonic inlets by highly swept microramps. *Journal of Propulsion and Power* 31(1), 133–143.

Zhou, Y. Y., Y. L. Zhao and Y. X. Zhao (2019). A study on the separation length of shock wave/turbulent boundary layer interaction. *International Journal of Aerospace Engineering 2019*.

Zukoski, E. E. (1967). Turbulent boundary-layer separation in front of a forward-facing step. *AIAA journal* 5(10), 1746–1753.

Zuo, F. Y., A. Memmolo, G. P. Huang and S. Pirozzoli (2019). Direct numerical simulation of conical shock wave–turbulent boundary layer interaction. *Journal of Fluid Mechanics* 877, 167–195.